# SIMULATION OF DEFORMATION AND HOT TEAR FORMATION USING A VISCO-PLASTIC MODEL WITH DAMAGE

C.A. Monroe [1], C. Beckermann[1], J. Klinkhammer [2]

[1] Dept. Mechanical and Industrial Engineering, University of Iowa, Iowa City, Iowa 52242, USA
[2] MAGMA Giessereitechnologie GmbH, Kackertstrasse 11, D-52072 Aachen, Germany

## Abstract

A three-phase model is presented that predicts solid deformation and damage as well as melt pressure, feeding flow and shrinkage porosity during metal casting. A visco-plastic constitutive theory with damage is used to model the solid deformation. Damage created by mechanically induced voiding is used as a hot tear indicator. The absence of liquid feeding determines when damage starts to form. The model has been implemented in general-purpose simulation codes. Novel steel casting experiments have been designed and performed which measure the deformation and force from solidification to shakeout. The measured and predicted deformations show generally good agreement with the simulation results. Furthermore, the damage predictions show good correspondence with hot tear indications on a radiograph of the test casting.

## 1. Introduction

In all casting processes, hot tearing and distortion during solidification and cooling are serious defects. Hot tears are cracks that initiate in the mushy zone at high solid fractions [1]. The two necessary conditions for hot tearing are (a) lack of liquid feeding and (b) tensile strain. First, liquid metal feeding is induced by solidification shrinkage. At high solid fractions, this liquid flow may be cut off because the permeability of the mushy zone becomes too low. Note that in shaped castings, a lack of liquid feeding can occur even at low solid fractions when a hot spot is present. The absence of liquid feeding signals the onset of shrinkage porosity formation. Second, non-uniform thermal contractions and mechanical restraints can cause the solid to strain. Such strains result in casting distortions and may also cause additional voiding. This additional voiding due to tensile strains is called damage. Hot tears are a manifestation of the damage that occurs during solidification.

In order to predict hot tearing and distortion, realistic and efficient models must be used to calculate the temperature, liquid flow, and strain fields during solidification and cooling of a casting. M'Hamdi *et al.* [2], Mathier *et al.* [3] and others have proposed two-phase models for calculating liquid flow and solid strain. Void nucleation is assumed to occur at a certain critical liquid pressure drop. After void nucleation, the volumetric part of the inelastic solid strain is integrated to obtain the void volume associated with the formation of a hot tear. However, the solid fraction is assumed to be a function of temperature only, and the effect of voids on the mechanical behavior of the solid (in the absence of liquid) is neglected.

In the present study, deformation and hot tearing during casting is modeled using a visco-plastic constitutive equation for the solid that accounts for the presence of voids (porosity). The liquid feeding flow and shrinkage porosity are predicted using the model first presented in Ref. [4]. Integration of the damage is started when the liquid feeding flow is predicted to be cut off.

The effects of solid deformation on liquid flow and of liquid pressure on solid deformation are neglected. Although the shrinkage porosity and the damage porosity are calculated separately, both porosities affect the mechanical behavior of the solid. The damage induced porosity is used as a hot tear indicator. The predictions of the present model are validated using a specially designed steel sand casting that allows for simultaneous force and displacement measurements during solidification and cooling.

## 2. Model Description

The volume averaged model accounts for the presence of three phases: solid ($s$), liquid ($l$), and porosity ($p$), such that the volume fractions add to unity, i.e., $g_s + g_l + g_p = 1$. While liquid is present, the solid fraction is assumed to be a unique function of the temperature, $T$, or $g_s(T)$. The porosity phase is split into two contributions, shrinkage and damage, i.e., $g_p = g_{p,sh} + g_{p,d}$. The shrinkage and damage porosity start to form when the liquid pressure falls to the negative of the critical capillary pressure for pore formation. The feeding flow, liquid pressure, and shrinkage porosity model used in the present study [4] neglects any contribution from the deformation of the solid. This model has previously been implemented in a general-purpose casting simulation code [5] that also provides the necessary heat transfer calculations.

The deformation of the solid and the mushy zone (above coherency) is modeled using the concept of an effective stress tensor, $\boldsymbol{\sigma}_s$, for porous solids. As in Ref. [3], the effects of the liquid pressure and liquid shear stress, as well as of gravity, on the solid deformations are neglected. Then, the solid momentum equation reduces to $\nabla \cdot \boldsymbol{\sigma}_s = 0$. The total strain is decomposed into three contributions: thermal, elastic, and visco-plastic. The thermal strain is calculated using the temperature dependent density; only the density changes below the solidus (100% solid) temperature are included. Hooke's law is used to determine the elastic strain. The elastic stiffness tensor is defined by the Young's modulus, $E$, and the Poisson ratio, $\nu$. Both elastic constants depend on temperature and solid fraction [6, 7]. The visco-plastic strain is calculated using an associative flow law. The flow law and the associated yield function are given in Table 1. In the yield function, the solid pressure and the von Mises stress are given by $p_s = -(\boldsymbol{\sigma}_s : \mathbf{1})/3$ and $q_s = 2|\boldsymbol{\sigma}_s + p_s\mathbf{1}|/3$, respectively.

A variety of yield functions are used to model plasticity of porous materials [8, 9, 10]. In the present study, the quadratic yield function from Cocks [8] given in Table 1 is adopted. The functions $A_1$ and $A_2$ depend on the volume fraction solid. When the solid fraction is equal to unity, this model reduces to a classical von Mises yield model. In order to account for void coalescence and solid coherency, the solid fraction used in the yield function is scaled according to the expression provided in Table 1. The solid fraction is only scaled below the so-called coalescence solid fraction, $g_s^{coal}$. For solid fractions below the coalescence solid fraction, voids coalesce and the mush rapidly weakens. The scaled solid fraction reaches zero at the so-called coherency solid fraction, $g_s^{coh}$. For solid fractions below the coherency solid fraction, the mush has no strength and stiffness. The dynamic yield stress is calculated from the power law given in Table 1, and includes both isotropic hardening and creep (rate-dependency). As shown in Table 1, the equivalent strain, $\varepsilon_{eq}$, and the equivalent strain rate, $\dot{\varepsilon}_{eq}$, are found from the scalar dissipation of energy.

The damage porosity is obtained by integrating the volumetric part of the visco-plastic strain over time (see Table 1). The integration starts at the time $t_f$, when the feeding flow is cut off. The damage porosity either reduces or increases the solid fraction. Once solidification is complete, the solid fraction used in the mechanical constitutive equations is reduced by the entire

porosity fraction, including shrinkage and damage. Hence, the effect of the voids on the mechanical behavior of the solid is taken into account.

The above model for the solid deformations was implemented in a user subroutine of the finite element software ABAQUS [11]. The numerical solution method uses an implicit-explicit integration scheme [9, 10]. Simulations were performed for the steel sand casting described below. The thermophysical properties of the steel were calculated using IDS [12]. The necessary mechanical properties were determined using published data [13, 14, 15]. The deformation of the sand mold, and the contact between the casting and the mold, were also simulated using ABAQUS.

Table 1. Equations and parameters used to model solid deformation.

| Equations |
|---|
| Flow law and Yield function: $\dot{\boldsymbol{\varepsilon}}_s^{vp} = \dot{\gamma}\dfrac{\partial f_Y}{\partial \boldsymbol{\sigma}_s}$ and $f_Y = q_s^2 + A_1 p_s^2 - A_2 \sigma_{dy}^2 \leq 0$, where $A_1 = \dfrac{9\left(1 - g_s^*\right)}{2\left(2 - g_s^*\right)\left(1 + m\right)\left(1 + 2\left(1 - g_s^*\right)/3\right)}$ and $A_2 = \left(1 + 2\left(1 - g_s^*\right)/3\right)^{-1}\left(g_s^*\right)^{2/(1+m)}$ Scaled solid fraction: $g_s^* = g_s^{coal}\left(g_s - g_s^{coh}\right)/\left(g_s^{coal} - g_s^{coh}\right)$ |
| Dynamic yield stress and equivalent strain: $\sigma_{dy} = \sigma_0\left(1 + \varepsilon_{eq}/\varepsilon_0\right)^n\left(1 + \dot{\varepsilon}_{eq}/\dot{\varepsilon}_0\right)^m$ and $\dot{\varepsilon}_{eq} = \boldsymbol{\sigma}_s : \dot{\boldsymbol{\varepsilon}}_s^{vp}/g_s\sigma_{dy}$ |
| Damage evolution: $g_{p,d} = \displaystyle\int_{t_f}^{t} g_s\dot{\boldsymbol{\varepsilon}}_s^{vp} : \mathbf{1}\,dt$ |

| Parameters and Constants | |
|---|---|
| **Quantity** | **Value** |
| Room Temperature 0.2% offset yield strength | 317 MPa |
| Coherency solid fraction | 0.5 |
| Coalescence solid fraction | 0.85 |
| 100% Solid Temperature and Anneal Temperature | 1415 °C |

### 3. Experimental Setup

Steel sand casting experiments were performed to validate the model. The unique feature of the experimental setup is that it allows for simultaneous force and displacement measurements during solidification and cooling of the casting. In addition, the casting can be mechanically restrained in order to induce relatively high stresses and hot tearing. As shown schematically in Figure 1, the casting consists of a 36" (0.914 m) long, 1" (25.4 mm) thick bar, referred to as "arm". Experiments were performed for arms widths of 1" (25.4 mm) and 2" (50.8 mm). The casting was gated using a runner that meets the bar at mid-length. This runner, referred to as "leg", creates a hot spot at the mid-length of the arm. A thermocouple was placed near the center of the leg. Leg widths of 1" (25.4 mm) and 2" (50.8 mm) were utilized in the experiments. Casting restraint was achieved by bolts that were embedded in the two ends of the arm. The bolts were connected to a flask that surrounds the mold. The restraining forces were measured using temperature compensated force gauges in each bolt. In one experiment, the bolts were removed

so that the arm can contract freely. Displacements were measured using two quartz rods connected to LVDTs. The quartz rods were embedded into the casting through tabs that were cast on the arm on both sides of the hot spot. As shown in Figure 1, the gap between the two tabs defines the gauge length for the displacement measurements. Depending on the restraint offered by the bolt/flask arrangement, the gap can either open (defined as positive gap displacement) or close. The mold was made of phenolic urethane bonded silica sand. The WCB low-alloy steel was poured at 2966$^o$F (1630$^o$C).
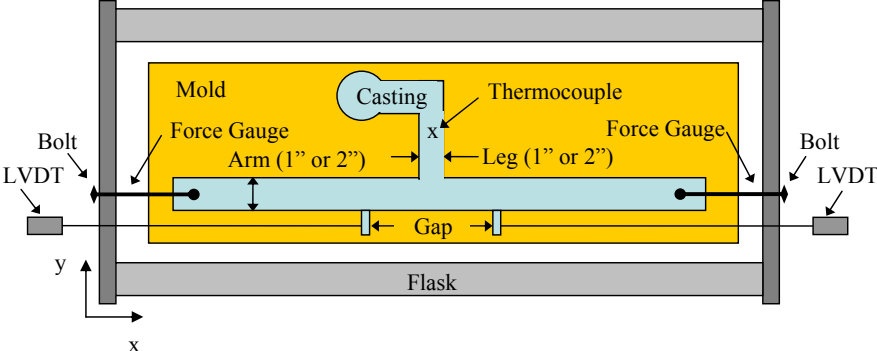


Figure 1.  Schematic of the test setup for the steel sand casting experiments.

## 4. Results and Discussion

An example of a comparison between measured and predicted temperatures is shown in Figure 2. The good agreement between the measurements and predictions was achieved by using a temperature dependent mold-metal interfacial heat transfer coefficient (not shown here due to space limitations). Similar agreement was obtained for all experiments.

Predicted mid-thickness shrinkage porosity fields are shown in Figure 3 for two cases: 2" arm with 2" leg; and 1" arm with 1" leg. In both cases, significant centerline shrinkage is predicted in the arm and leg, since the castings are not risered. In addition, a large amount of shrinkage porosity can be observed at the hot spot that is present near the arm-leg junction. This porosity pattern is as expected. Recall that



Figure 2.  Comparison of measured and predicted temperatures.

the time during solidification at which the shrinkage porosity is predicted to start forming at a particular location in the casting is used in the stress analysis as the start time for the integration of the damage.
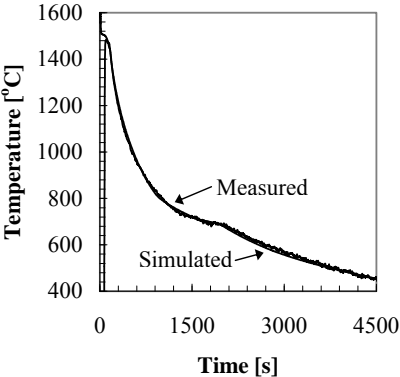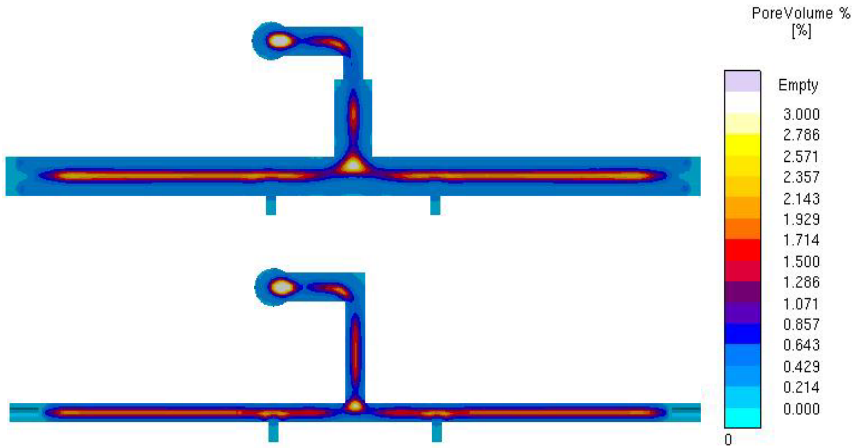
Figure 3. Predicted mid-thickness shrinkage porosity fields for the 2" wide arm/leg (top) and the 1" wide arm/leg (bottom) castings.

One casting was poured unrestrained, without the bolts, the results for which are shown in Figure 4. The measured gap displacement as a function of time is shown in Figure 4(b). It can be seen that, as expected, the gap closes (i.e., the displacement is negative) due to thermal contraction of the arm. However, at about 1100 s after pouring, the gap starts to open by a small amount. This opening can be attributed to the expansion associated with the austenite to pearlite phase transformation. The transformation is complete at approximately 1600 s, after which the
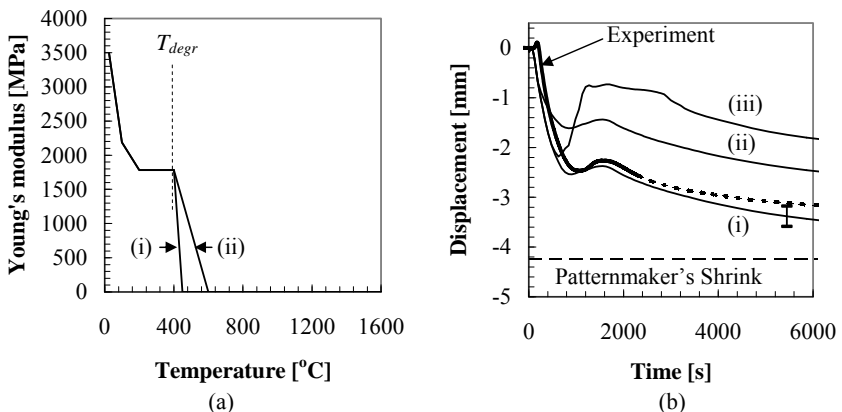


Figure 4. (a) Variation of Young's modulus of the mold with temperature. (b) Comparison of measured and predicted gap displacement variations for the unrestrained casting; predicted results are shown for three different cases: (i) baseline mold stiffness with degradation; (ii) higher mold stiffness at high temperatures, with degradation; (iii) baseline mold stiffness but no degradation upon cooling.

gap starts to close again. As indicated in Figure 4(b), the final measured gap displacement, when the casting is at room temperature, is significantly smaller than the value anticipated from the so-called Patternmaker's Shrink rule for free contraction of steel castings (2.08%). This effect can be attributed to the displacement of the tabs being hindered by the mold between the two tabs. This hindrance is a strong function of the mold stiffness. Simulations were performed for three different mold stiffness variations with temperature. As plotted in Figure 4(a), the baseline mold stiffness variation [case (i)] shows a sharp drop to zero at approximately 400°C. The drop occurs above the binder degradation temperature, $T_{degr}$. Once the binder is degraded, the mold does not regain stiffness when it cools to lower temperatures. This baseline mold stiffness variation produces excellent agreement between the measured and predicted gap displacements, as shown in Figure 4(b). In case (ii), degradation is also included, but the drop in the mold stiffness above $T_{degr}$ is not as steep and the stiffness does not vanish until about 600°C. This mold stiffness variation results in smaller predicted gap displacements that are in disagreement with the measurements. In case (iii), the same mold stiffness variation as in case (i) is used, but the mold is allowed to regain its stiffness upon cooling, regardless of how high a temperature it had reached previously. This mold stiffness variation also results in incorrect gap displacement predictions [Figure 4(b)].

Next, results are provided for two restrained castings: 2" arm with a 2" leg; and 1" arm with a 1" leg. The measured forces for these two castings are shown in Figure 5. In each experiment, the force measurements at the two bolts were very similar, and only the average values are plotted. It can be seen that the forces begin to increase quickly after the solidification of the arms. The drop in the forces at intermediate times can again be attributed to the expansion associated with the austenite to pearlite transformation. Note that the expansion occurs at different times for the two experiments, since the castings have much different cooling rates. After the phase transformation is completed, the forces increase again. These measured force variations are used as a boundary condition at the end of the arms in the deformation simulations.
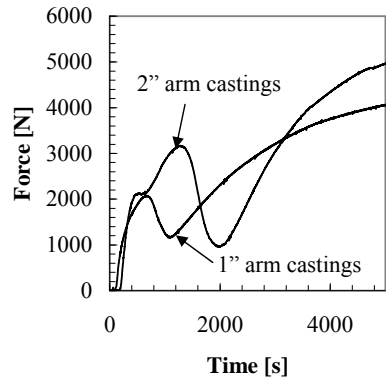


Figure 5. Variation of the average force in the restrained castings with time.

Comparisons of the measured and predicted gap displacements for the restrained castings are shown in Figure 6. Good agreement is obtained for the 2" arm/leg restrained casting [Figure 6(a)]. For this casting the gap displacements are similar to the ones for the unrestrained casting [Figure 4(b)], indicating that the stresses in the 2" wide arm are too low to cause significant yielding. For the 1" arm/leg casting, results from two separate, but nominally identical experiments are included in Figure 6(b). The measured gap displacements for the two experiments are similar and demonstrate little overall gap opening or closing. This indicates that the restraint induces significant yielding. Since the measured forces are of a similar magnitude in the 2" and 1" arm/leg (Figure 5) experiments, the stresses are approximately twice as high in the 1" wide arm as in the 2" wide arm. The simulation of the 1" arm/leg experiments predicts a larger gap closing than measured. Reasons for the disagreement may include uncertainties in the high-temperature mechanical properties and inaccurate modeling of crack propagation.
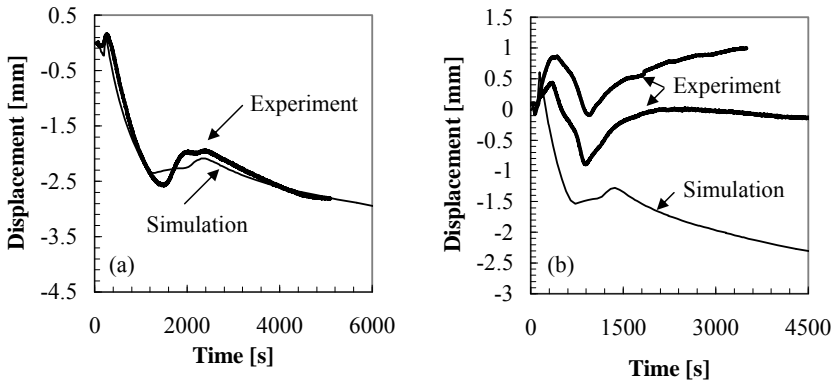
Figure 6. Comparison of measured and predicted gap displacements for the restrained castings; (a) 2" arm/leg, (b) 1" arm/leg.

Figure 7(a) shows the predicted distortions (magnified by a factor of five) and damage porosity field for the restrained 2" arm/leg casting. The casting can be seen to contact the mold at several locations along the metal-mold interface, while at other locations a gap forms. The predicted damage is mostly confined to the hot spot at the junction between the arm and the leg. A radiograph of the casting is provided in Figure 7(b). It shows a large crack in the center of the hot spot region, which is in good agreement with the damage prediction. The smaller indications along the centerline of the arm correspond well with the predicted porosity. Although this comparison is not of a quantitative nature, it illustrates the highly coupled nature of the shrinkage porosity and the damage porosity.
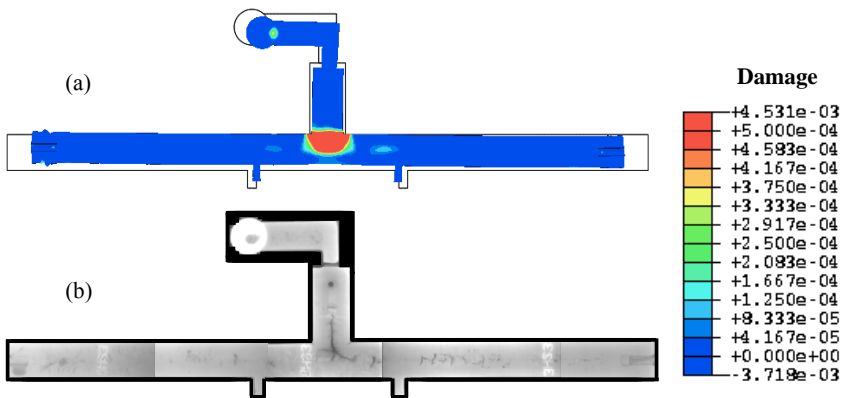


Figure 7. Results for the restrained 2" arm/leg casting. (a) Predicted distortions (five times magnified) and damage porosity field; (b) radiograph of the casting.

## 5. Conclusions

A model for the deformation and damage accumulation during solidification and cooling of shaped castings has been developed. Novel steel sand casting experiments, which allow for simultaneous displacement and force measurements, are used to validate the model predictions. Good overall agreement is obtained. However, some uncertainty remains regarding the high temperature mechanical properties used in the simulations. The comparisons also illustrate the importance of accurate modeling of the mechanical behavior of the mold, including binder degradation. Additional work is needed to verify the model for situations where significant hot tearing occurs. Such hot tearing significantly affects the subsequent deformation of a casting.

## Acknowledgements

## References

1. M. Rappaz, J.-M. Drezet, and M. Gremaud, "A new hot-tearing criterion," *Metall. Mater. Trans. A*, 30A (1999), 449-455.
2. M. M'Hamdi, A. Mo, and H. G. Fjaer, "Tearsim: A two-phase model addressing hot tearing formation during aluminum direct chill casting," *Metall. Mater. Trans. B*, 37 (2006), 3069-3083.
3. V. Mathier, J.-M. Drezet, and M. Rappaz, "Two-phase modeling of hot tearing in aluminum alloys using a semi-coupled approach," *Modelling Simul. Mater. Sci. Eng.*, 15, (2007), 121-134.
4. K. Carlson, Z. Lin, R. Hardin, C. Beckermann, G. Mazurkevich, and M. Schneider, "Modeling of porosity formation and feeding flow in steel casting," in *Modeling of Casting, Welding, and Advanced Solidification Processes X*, TMS (2003), 295-302.
5. MAGMAsoft v4.5, MAGMA GmbH, Aachen, Germany
6. R. A. Hardin and C. Beckermann, "Effect of porosity on the stiffness of cast steel," *Metall. Mater. Trans. A*, 38 (2007), 2992-3006.
7. A. Roberts and E. Garboczi, "Elastic properties of model porous ceramics," *Journal of the American Ceramic Society*, 83 (2000), 3041-3048.
8. A. C. F. Cocks, "Inelastic deformation of porous materials," *J. Mech. Phys. Solids*, 37 (1989), 693-715.
9. E. B. Marin and D. L. McDowell, "A semi-implicit integration scheme for rate-dependent and rate-independent plasticity," *Computers and Structures*, 63 (1997), 579-600.
10. P. Sanchez, A. Huespe, and J. Oliver, "On some topics for the numerical simulation of ductile fracture," *Int. J. of Plasticity*, 24 (2008), 1008-1038.
11. ABAQUS v6.7-1, D S Simulia, Dassault Systemes
12. J. Miettinen, "Calculation of solidification-related thermophysical properties for steels," *Metall. Mater. Trans. B*, 28A (1997), 281-297.
13. P. J. Wray, *Modeling of Casting and Welding Processes*, Ringe, NH: AIME Conference Proceedings (1980), 245-257.
14. P. J. Wray, "Effect of carbon content on the plastic flow of plain carbon steels at elevated temperatures," *Metall. Mater. Trans. A*, 13A (1982), 125.
15. *High Temperature Property Data: Ferrous Alloys*, ASM International, Metals Park, OH (1988).